Available online at www.sciencedirect.com
SCIENCE DIRECT®
International Journal of Heat and Mass Transfer 48 (2005) 4384–4396
International Journal of HEAT and MASS TRANSFER
www.elsevier.com/locate/ijhmt

Numerical investigations on cold gas dynamic spray process with nano- and microsize particles

Tien-Chien Jen [a,*], Longjian Li [b], Wenzhi Cui [b], Qinghua Chen [b], Xinming Zhang [b]

[a] Department of Mechanical Engineering, University of Wisconsin, Milwaukee, Milwaukee, WI 53211, USA
[b] College of Power Engineering, Chongqing University, Chongqing 400044, China

Received 7 June 2004; received in revised form 12 May 2005
Available online 20 July 2005

Abstract

The particle velocity in cold gas dynamic spraying (CGDS) is one of the most important factors that can determine the properties of the bonding to the substrate. In this paper, the acceleration process of microscale and sub-microscale copper (Cu) and platinum (Pt) particles inside and outside De-Laval-Type nozzle is investigated. A numerical simulation is performed for the gas-particle two phase flow with particle diameter ranging from 100 nm to 50 μm, which are accelerated by carrier gas nitrogen and helium in a supersonic De-Laval-type nozzle. The carrier gas velocity and pressure distributions in the nozzle and outside the nozzle are illustrated. The centerline velocity for two types of particles, Pt and Cu, are demonstrated. It is observed that the existence of the bow shocks near the substrate prevents the smaller size particles (less than 0.5 μm) from penetrating, thus leads to poor coating in the actual practices. Furthermore, the extended straight section may have different optimal length for different size particles, and even may be unnecessary for sub-microsize particles.

Keywords: Cold gas dynamic spraying (CGDS); Micro- and sub-microsize particles; Numerical simulation

1. Introduction

The feasibility of a low temperature CGDS material deposition technology was demonstrated based on the introduction of 1-μm to 50-μm solid metal particles into a gas stream accelerated to supersonic velocities, and subsequently deposited on the substrate [1]. CGDS process has been considered as a promising new process compared to the well-established thermal spraying process. In CGDS, the deleterious effects of high temperature oxidation, evaporation, melting, crystallization, residual stresses, debonding and gas release caused by the commonly used thermal spraying processes can be avoided. Moreover, the advantages of this approach include the high bonding strength of the particle, high production rate due to high deposition rate (deposition efficiencies of up to 80%), and ability to recycle the powders.

In earlier works, one-dimensional isentropic flow model was generally used to analyze the dynamics of dilute two-phase (feed-powder particles suspended in a

* Corresponding author. Tel.: +1 414 229 2307; fax: +1 414 229 6958.
E-mail address: jen@cae.uwm.edu (T.-C. Jen).

0017-9310/$ - see front matter © 2005 Elsevier Ltd. All rights reserved.
doi:10.1016/j.ijheatmasstransfer.2005.05.008

Nomenclature

A	area [m^2]
A_p	surface area of the particle [m^2]
c_p	specific heat capacity [J/(kg K)]
$C_{\varepsilon 1}$, $C_{\varepsilon 2}$, C_μ	turbulent model constant
D_p	particle diameter [m]
F_D	drag force per unit particle mass [N/kg]
h	convective heat transfer coefficient [W/m^2 K]
k	turbulent kinetic energy [m^2/s^2]
m_p	mass of the particle [kg]
p	pressure [N/m^2]
Pr	molecular Prandtl number
R	ideal gas constant
Re	Reynolds number
T	temperature [K]
T	time [s]
u_i	velocity component in i-direction ($i = 1, 2, 3$) [m/s]
x_i	Cartesian coordinate in the i-direction ($i = 1, 2, 3$] [m]

Greek symbols

Γ	thermal conductivity [W/(m K)]
ε	dissipation ratio of turbulent kinetic energy [m^2/s^2]
μ	viscosity [kg/(ms)]
μ_{eff}	effective viscosity [kg/(ms)]
ρ	density of fluid [kg/m^3]
α_T, α_k, α_ε	inverse effective Prandtl number for energy equations, T, k and ε

Subscripts

i, j, k	general spatial indices
eff	turbulent effective parameters
mol	molecule property
p	particle property
t	turbulent quantity

carrier gas) flow during the cold-gas dynamic-spray process. McCune et al. [2] and Dykhuizen and Smith [3] have modeled the gas dynamics of CGDS, using a simplified one-dimensional flow model, and concluded that in order to increase the particle impact velocity, a longer nozzle, smaller particles, higher operating pressure or a lower molecular weight carrier gas should be used. But some complex phenomena such as shock wave, separating flow and etc. could not be analyzed with the one-dimensional model; thereby the numerical method was required to solve the governing equations in the spray process.

Over past few decades, there were many researches on numerical simulation of heat and mass transfer in the conventional spray process, such as water spray [4], and fuel spray [5–7] in the engine. The numerical approaches were also widely used in the analyses of the thermal spray (TS) to understand the heat and mass transfer mechanisms in flame spray [8], oxygen-fuel thermal spray [9], thermal plasma spraying [10]. Eidelman and Yang [11,12] developed a three-dimensional compressible, turbulent flow Navier–Stokes model and a multi-phase particle flow model in Lagrangian formulation for the thermal spray, which was used for analysis of the JP-5000 TS gun gas and coating powder flow conditions. Modeling and analysis of particle/turbulent eddies interaction were performed, with a view on improving TS gun performance through control of its parameters.

In recent years, there were also many researches on numerical simulation of cold gas dynamics spray process. First, the nozzle geometry is important either in the high-velocity oxygen-fuel (HVOF) thermal spray process or in the cold spray process. Sakaki and Shimizu [13] carried out numerical simulation and experiments to investigate the effect of the entrance geometry of the gun nozzle on the HVOF process, the study results also could be applied to the nozzle design for the cold spray method. The numerical and experimental research results for wedge-shaped supersonic nozzles, conducted by Alkhimov et al. [14], showed that for a nozzle with particular dimensions for a given type of particles that produces the maximum possible particle velocity at the moment of impact on a target surface. In the research discussed above, the numerical simulation was mainly aimed at the supersonic flow inside the nozzle. Actually, the acceleration performance of particles is also strongly affected by the flow outside the nozzle.

Wang et al. [15] employed the extended-pressure correction algorithm to solve Navier–Stokes equation of the turbulence, and the staggered grid was adopted to reduce the numerical diffusion, and the high resolution ratio discretization was utilized to improve the shock-capture. The numerical analysis was used to direct and optimize the cold spray experiment. Wang's work was mainly aimed at the simulation of flow outside the nozzle exit. Li and Li [16] systematically investigated the effects of the parameters involved in cold spray on the acceleration of particles by a CFD code. The parameters involved include nozzle geometry parameters, processing parameters and properties of spray particles. It was found that the carrier gas type,

operating pressure and temperature are main processing parameters, which influence particle velocity. As for nozzle geometry, the expansion ratio and divergent section length of spray gun nozzle show significant effects on particle velocity. Moreover, the density, size and morphology of powder also have significant effects on particle velocity. The effects of those main parameters are summarized in a comprehensive equation obtained through nonlinear regression of the simulated results for the estimation of particle velocity. Li et al. [17] conducted numerical simulations for gas–solid two-phase flows for an experimental coating of an industrial booth to study the effect of the coating powder size on the performance of the coating process. In order to increase the coating process efficiency and coating quality, different coating parameters, such as the size of the coating part, the distance between the coating part and the spray gun, the air flow rate and particle flow rate from the spray gun, the position of the pattern adjust sleeve of the spray gun, and the electrostatic field were accounted for in their simulations. The airflow field is obtained by solving three-dimensional Navier–Stokes equations with standard k–ε turbulence model and non-equilibrium wall function. The second phase, the coating powder, consists of spherical particles and is dispersed in the continuous phase, the air. In addition to solving transport equations for the air, the trajectories of the particles are calculated by solving the particle motion equations using Lagrangian method.

By using CFD (Computational Fluid Dynamics) program FLUENT, Yen [18] used nitrogen and helium as carrier gases to simulate the acceleration process of copper particles diameter varying from 5 μm to 25 μm with the inlet conditions at $P_0 = 2.5$ MPa and $T_0 = 673$ K. He found that the particle velocity is a controlling factor that can determine the properties of the bonding to the substrate. Also, carrier gas helium travels 2.5 times faster than nitrogen in supersonic nozzle. Furthermore, smaller particles travel faster than larger particles, and increasing the gas pressure and temperature can raise the particle velocity. He also noted that particles travel faster in an extended nozzle.

In previous researches on CGDS, the sprayed particle diameter is usually less than 1 μm. In this study our primary motivation is to extend CGDS technology to nano-scale particle size. If successful, this research can certainly open a door for more cross-disciplinary applications of nano- and CGDS technology such as cold surface coating technology. However, before developing this new nano-particle CGDS coating technology, we need to understand the details of nano-particles transport process in a supersonic gas stream inside and outside the nozzle, that imply our simulation model will include the whole zone from the inlet of the nozzle to the substrate. The key issue for a successful CGDS technique for nano-particles coating is the bonding on the substrate. In order to bond powder particles to the substrate upon impact, the particles need to attain enough momentum. Therefore, for a certain diameter of particles of a certain material, its velocity gained in the supersonic gas stream must be greater than a critical velocity for a bond to form; below this critical velocity particle either bounce off the substrate or wear the substrate material off. This critical velocity is approximately 450 m/s for copper powder with 5 μm diameter impinging on copper substrate, as shown in McCune et al. [2].

To provide information on the development of velocity to smaller particles along the gas stream, a numerical calculation has been performed using nitrogen and helium as carrier gas to accelerate the copper and platinum particles with diameters varying from 100 nm to 50 μm in a nozzle with a ratio of expansion of $A_E/A_* = 28.4$. The carrier gas has an inlet pressure $p_0 = 2.0$ MPa and a inlet temperature $T_0 = 773$ K.

2. Mathematical model

The physical configuration of the nozzle is schematically shown in Fig. 1. The geometries of the nozzle exactly match the test nozzle of the experimental apparatus, which has been established in our laboratory. This paper will only focus on the numerical analysis on the CGDS process. The computational domain consists of a De-Laval-Type (convergent–divergent) nozzle connected with a straight pipe, which is used to further accelerate the particle and the region from the outlet of the nozzle to substrate. The RNG k–ε model proposed by Yakhot and Orszag [19] is chosen for modeling the turbulent flow in the pipe. The RNG k–ε model was derived using a rigorous statistical technique (called renormalization group theory), which has an additional term in its equation that significantly improves the accuracy for rapidly strained flows. This feature makes the RNG k–ε model more accurate and reliable for a wider class of flows than the standard k–ε model. In the three-dimensional Cartesian coordinate system, the time-averaged partial differential governing equations for compressible flows of ideal gas are written in tensor form as follows:

Mass

$$\frac{\partial(\rho u_i)}{\partial x_i} = 0 \tag{1}$$

Momentum

$$\frac{\partial}{\partial x_j}(\rho u_i u_j) = \frac{\partial}{\partial x_j}\left[\mu_{\text{eff}}\left(\frac{\partial u_i}{\partial x_j} + \frac{\partial u_j}{\partial x_i}\right) - \frac{2}{3}\mu_{\text{eff}}\frac{\partial u_k}{\partial x_k}\right] - \frac{\partial p}{\partial x_i} \tag{2}$$

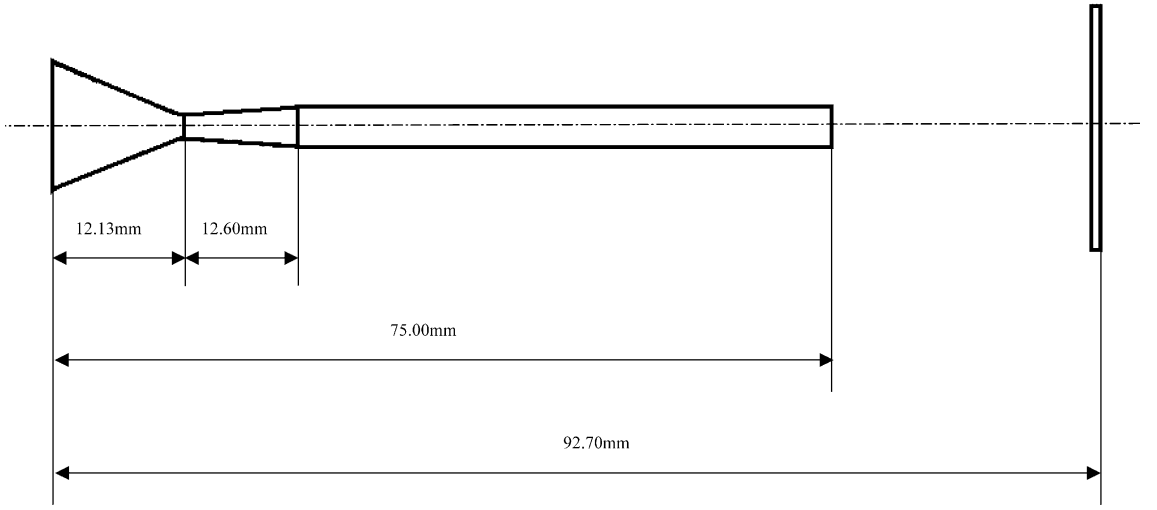

Fig. 1. Schematic of the nozzle pipe.

Energy

$$\frac{\partial}{\partial x_i}(\rho u_i c_p T) = \frac{\partial}{\partial x_i}\left[\alpha_T\left(\mu_{\text{eff}}\frac{\partial T}{\partial x_i}\right)\right] + \frac{\partial u_i}{\partial x_j}\left[\mu_{\text{eff}}\left(\frac{\partial u_i}{\partial x_j}+\frac{\partial u_j}{\partial x_i}\right)-\frac{2}{3}\frac{\partial u_k}{\partial x_k}\right] \tag{3}$$

Turbulent kinetic energy

$$\frac{\partial}{\partial x_i}(\rho u_i k) = \frac{\partial}{\partial x_i}\left[\left(\alpha_k \mu_{\text{eff}}\frac{\partial k}{\partial x_i}\right)\right] + \mu_t S^2 - \rho\varepsilon \tag{4}$$

Dissipation rate of turbulent kinetic energy

$$\frac{\partial}{\partial x_i}(\rho u_i \varepsilon) = \frac{\partial}{\partial x_i}\left[\left(\alpha_\varepsilon \mu_{\text{eff}}\frac{\partial \varepsilon}{\partial x_i}\right)\right] + C_{1\varepsilon}\frac{\varepsilon}{k}\mu_t S^2 - C_{2\varepsilon}\rho\frac{\varepsilon^2}{k} - R \tag{5}$$

For compressible flows, the ideal gas law is written in the following form:

$$p/\rho = RT \tag{6}$$

The effective viscosity μ_{eff} is calculated by the following equation:

$$\mu_{\text{eff}} = \mu_{\text{mol}}\left[1+\sqrt{\frac{C_\mu}{\mu_{\text{mol}}}}\frac{k}{\sqrt{\varepsilon}}\right]^2 \tag{7}$$

where μ_{mol} is the molecular viscosity. Eq. (7) indicates that the RNG $k-\varepsilon$ model yields an accurate description of how the effective turbulent transport varies with the effective Reynolds number (or eddy scale), allowing accurate extension of the model to low-Reynolds-number and near-wall flows. The coefficients, α_T, α_k and α_ε, in Eqs. (3)–(5) are the inverse effective Prandtl numbers for T, k, and ε, respectively. They were computed using the following formula:

$$\left|\frac{\alpha-1.3929}{\alpha_0-1.3929}\right|^{0.6321}\left|\frac{\alpha+2.3929}{\alpha_0+2.3929}\right|^{0.3679} = \frac{\mu_{\text{mol}}}{\mu_{\text{eff}}} \tag{8}$$

where α_0 is equal to $1/Pr$, 1.0 and 1.0, for the computation of α_T, α_k and α_ε, respectively. S in Eqs. (4) and (5) is the modulus of the mean rate-of-strain tensor, S_{ij}, which is defined as $S = \sqrt{2S_{ij}S_{ij}}$, where, $S_{ij} = \frac{1}{2}\left(\frac{\partial u_i}{\partial x_j}+\frac{\partial u_j}{\partial x_i}\right)$. R in Eq. (5) is given by

$$R = \frac{C_\mu \rho \eta^3(1-\eta/\eta_0)}{1+\zeta\eta^3}\cdot\frac{\varepsilon^2}{k} \tag{9}$$

where $\eta = S\cdot k/\varepsilon$, $\eta_0 \approx 4.38$, and $\zeta = 0.012$. The model constants C_μ, $C_{1\varepsilon}$ and $C_{2\varepsilon}$ are equal to 0.085, 1.42, and 1.68, respectively.

In the near wall zone, the two-layer-based, non-equilibrium wall function was used for the near-wall flow treatment. This method requires some consideration of mesh, i.e., the cell adjacent to the wall should be located to ensure that the parameter $y^+(\equiv ru_\tau y/\mu)$ or $y^*\left(\equiv\frac{\rho C_\mu^{1/4}k_P^{1/2}y_P}{\mu}\right)$ falls into the 30–60 range. In the present study, y^+ was adapted into the 30–60 range.

The particle is treated as discrete phase dispersed in the continuous phase (gas), and the motion of which is computed using a Lagrangian formulation that includes the discrete phase inertia, hydrodynamic drag, the force of gravity, heating of the discrete phase as well as the effects of turbulence on the dispersion of particles due to turbulent eddies present in the continuous phase. The trajectory of a discrete phase particle is predicted by integrating the force balance on the particle. This force balance equates the particle inertia with the forces acting on the particle, and can be written (for the x direction in Cartesian coordinates) as

$$\frac{du_p}{dt} = F_D(u - u_p) + g_x(\rho_p - \rho)/\rho_p + F_x \quad (10)$$

where F_D is the drag force per unit particle mass, which is equivalent to $F_D = \frac{18\mu}{\rho_p D_p^2}\frac{C_D Re}{24}$. Here u is the fluid phase velocity, u_p is the particle velocity, μ is the molecular viscosity of the fluid, ρ is the fluid density, ρ_p is the density of the particle, and D_p is the particle diameter. Re is the relative Reynolds number (i.e. particle Reynolds number), which is defined as

$$Re = \frac{\rho D_p |u_p - u|}{\mu} \quad (11)$$

The drag coefficient C_D, can be taken from:

$$C_D = a_1 + \frac{a_2}{Re} + \frac{a_3}{Re^2} \quad (12)$$

Here, a_1, a_2 and a_3 are constants (see Appendix A) that apply for smooth spherical particles over several ranges of Re given by Morsi and Alexander [20]. For

Fig. 2. N_2 gas isotaches of in the nozzle.

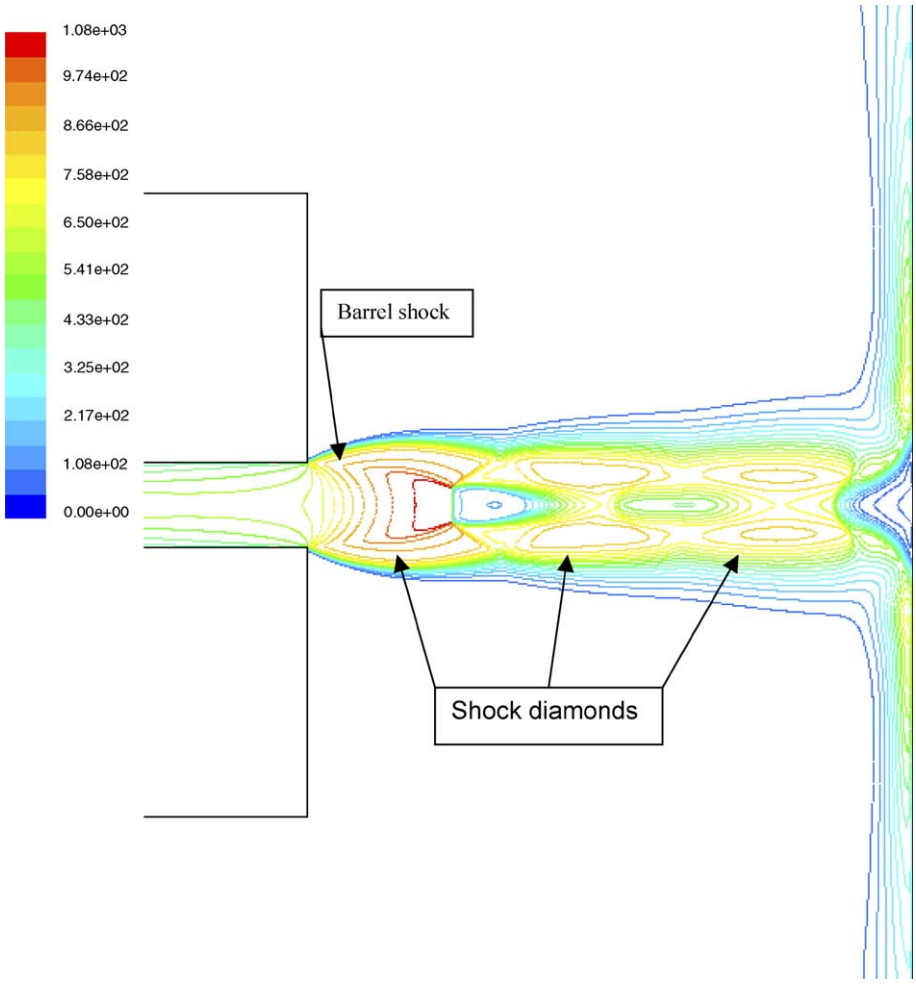

Fig. 3. The velocity contour of N_2 outside the nozzle.

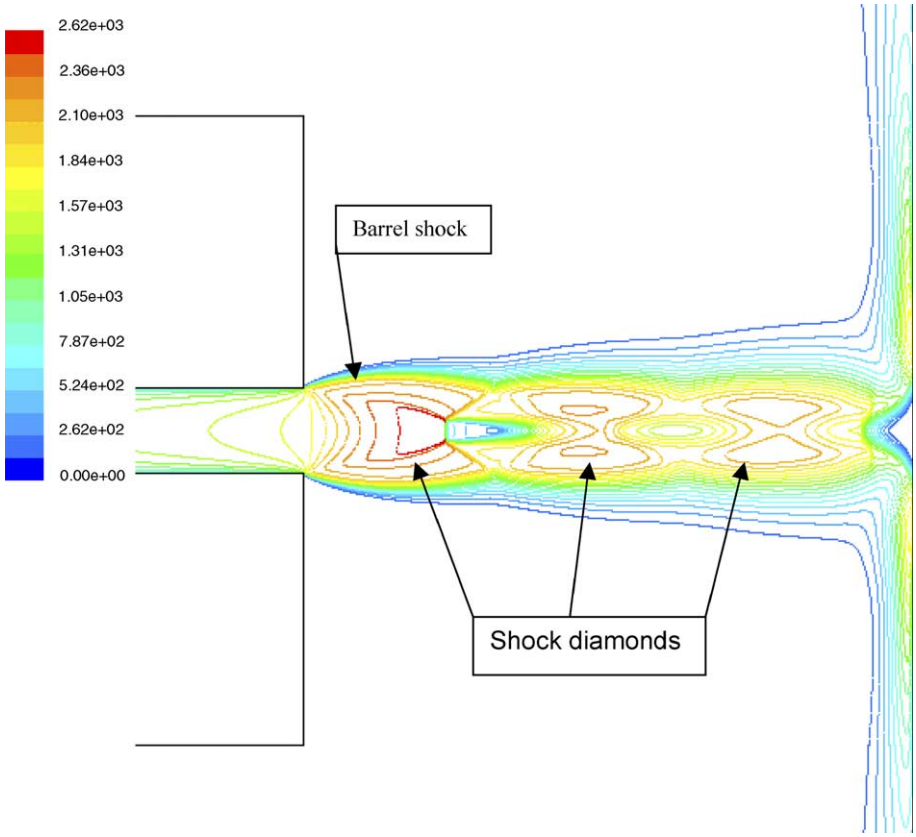

Fig. 4. The velocity contour of He outside the nozzle.

sub-micron particles, a form of Stokes' drag law is available [21]. In this case, F_D is defined as $F_D = \frac{18\mu}{\rho_p D_p^2 C_C}$. The factor C_C is the Cunningham correction to Stokes' drag law:

$$C_C = 1 + \frac{2\lambda}{D_p}\left[1.25 + 0.4\exp\left(-1.1(D_p/2\lambda)\right)\right] \quad (13)$$

where λ is the molecular mean free path. The third term on the right-hand side of Eq. (10) incorporates additional forces (F_x) in the particle force balance. For sub-micron particles, the Brownian force and the Saffman's lift force [22] are taken into consideration. The effects of Brownian force and the Saffman's lift force are optionally included in the additional force term only in some special computation domain where the flow is Stokes flow.

In order to predict the dispersion of the particles due to turbulence, a stochastic method is used to determine the instantaneous gas velocity. In the stochastic tracking approach, the turbulent dispersion of particles is calculated by integrating the trajectory equations for individual particles, using the instantaneous fluid velocity, $u + u'$, along the particle path during the numerical integration.

3. Numerical computation

The governing equations for the compressible flows and particle motion inside and outside the nozzle are solved using a control-volume finite element method (CVFEM). The second-order upwinding scheme proposed by Rhie and Chow [23] was selected for the discretization of the convection term in the governing equations. A structured non-uniform grid system has been used to discretize the computation domain. For a compressible flow with weak shocks, the gradient adaption is used for the solution of the supersonic flow. The pressure gradients in the solution are used to adapt the grid. The calculations on the adapted grid result in a much sharper definition of the shocks. The grid independence was investigated in the analysis by adopting different grid distributions. The grid independence test indicated that the grid system of 500,000 is sufficient for a satisfactory solution.

Based on the assumption that the particle phase is present at a low mass and momentum loading, in which the continuous phase is not impacted by the presence of the discrete phase, the two different phases can then be

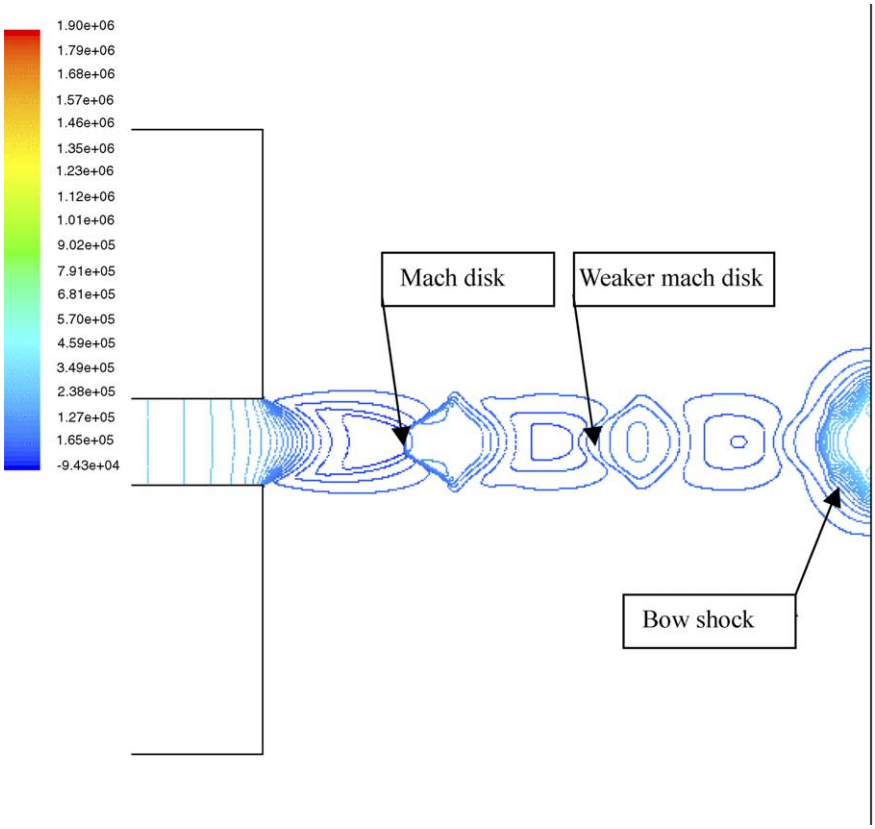

Fig. 5. The pressure contour of N_2 outside the nozzle.

uncoupled to solve iteratively. This is a two-step procedure. First, the SIMPLE method is used to solve the continuous phase flow field. Then the particle trajectories for discrete phase of interest are calculated. In this paper, the flow media are nitrogen (N_2) and helium (He), the particle phases are copper (Cu) and platinum (Pt), respectively.

4. Results and discussion

Fig. 2 shows the isotaches of the N_2 carrier gas in the nozzle. It can be seen that the velocity reaches its maximum at the exit of the divergent section. At the location of the connection between the divergent section and the following straight section, the supersonic flow is forced to turn around a small angle. Therefore, cone-shape weak shocks (compression waves) occur, and the multiple reflections of the shock waves on wall and the centerline of the nozzle result in the centerline velocity fluctuations (see Figs. 8 and 10 for details). And the friction in the straight section causes the gas velocity decreases significantly.

As the supersonic flow exits the nozzle, shock diamonds are formed due to the pressure difference between the supersonic flow and the ambient atmosphere. The adjustment of supersonic flow to the atmospheric pressure is through shock waves; these are initially either oblique shocks (lip shock) or expansion fans (barrel shock), which correspond to overexpanded or underexpanded jet respectively. As the waves reflect from the edges of the jet, they change polarity (i.e., an expansion fan reflects as a compression wave and a compression shock reflects as an expansion fan.). Thus, both types of shocks will simultaneously be present. Figs. 3 and 4 depict the underexpanded flow situations for N_2 and He, respectively. Barrel shock appears outside the nozzle first because the flow static pressure at the exit is higher than the back pressure, so the flow must be expanded to eventually reach the back pressure. It can also be seen from Figs. 3 and 4 that outside of the jet core the densely spaced contour levels indicates the shear layers developing at the jet boundary. Note that the flow at this region entrains the gas outside the shear layers, therefore, the shear layer grows and it penetrates into the jet core. In Figs. 5 and 6, the pressure distribution of

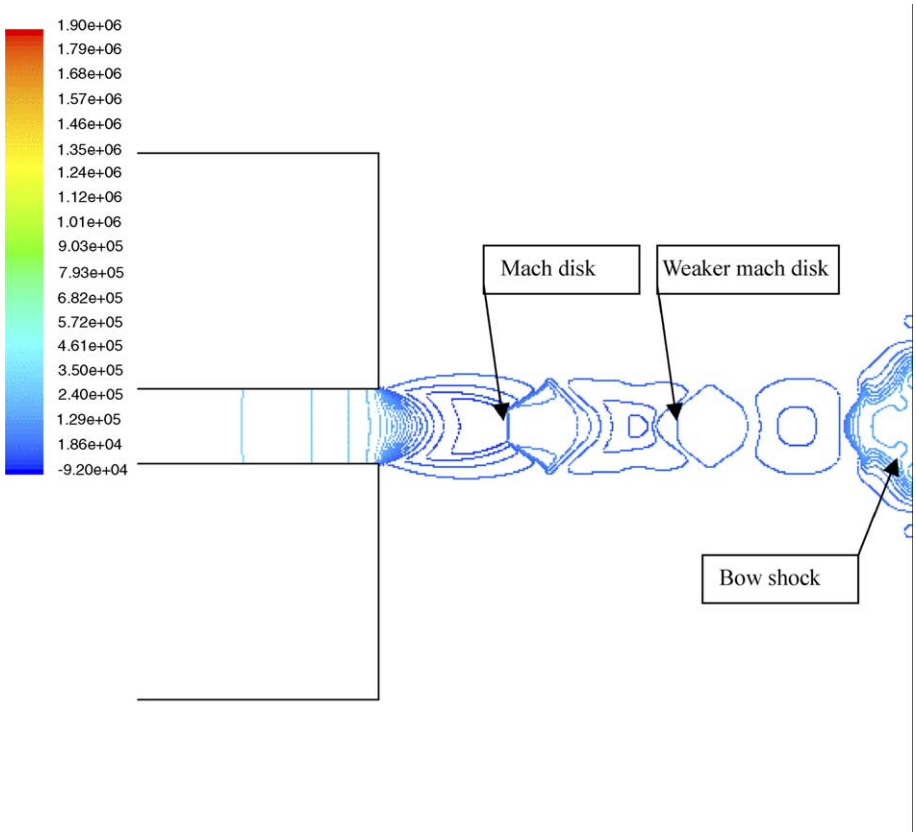

Fig. 6. The pressure contour of He outside the nozzle.

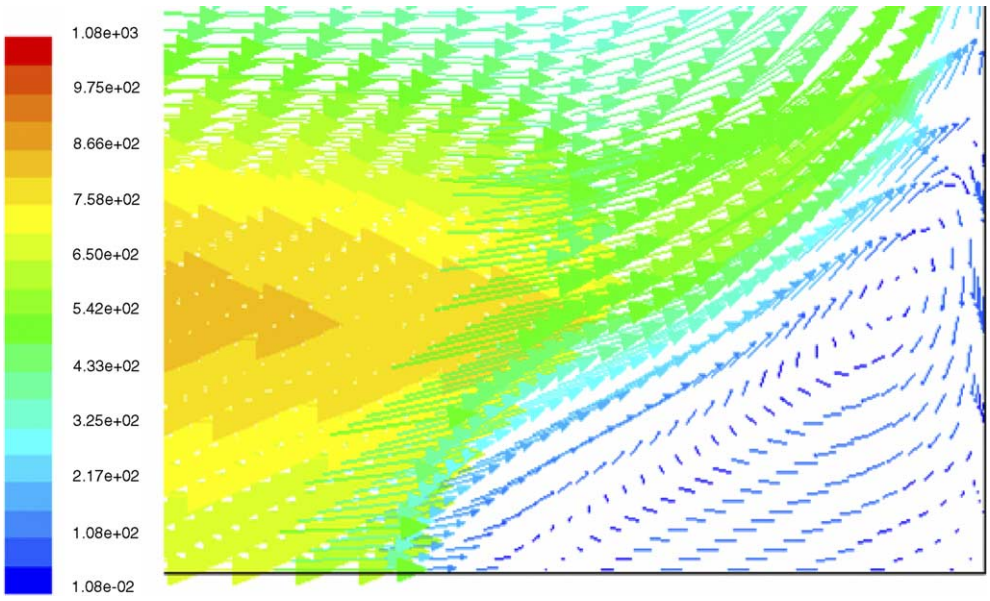

Fig. 7. The vortex exists in the place between bow shock and substrate (N_2).

the underexpanded N_2 and He jets is characterized by a sharp shock front and pressure peak close to the jet exit. Between nozzle exit and the substrate, there exists a well-formed Mach disk located close to the nozzle exit, a subsequent second weaker Mach disk and a Bow shock formed on the substrate. The contour plots show that the low static pressure before Mach disk leads to rapid compression and deceleration of flow gas at the centerline as the gas penetrates into the Mach disk; and high static pressure after the Mach disk immediately leads to rapid gas expansion and acceleration till it reaches the next oblique shock of the second shock disk. The both pressure contours of N_2 and He gas jet indicate that there is a steep pressure increase across the Bow shock. Unlike region behind the Mach disk, the pressure in this area closed by Bow shock and the substrate is much higher; and gas flow pattern in this region is also quite different. Fig. 7 illustrates the vector plots of the velocity distribution in this region. It is observed that the flow direction around the centerline is opposite the direction of the main jet stream because of the vortex formed in this closed region.

Figs. 8 and 9 depict the centerline velocities of copper and platinum particles on centerline with different diameters in N_2 carrier gas stream. For copper particles the cone-shape weak shocks in the nozzle, the Mach disk and Bow shock outside the nozzle almost have no effect on the acceleration of copper particles with diameter more than 5 μm. Although the cone-shape weak shocks (inside the nozzle) cannot slow down the smaller particles, such as 1 μm and 0.5 μm diameter particles, the Mach disk and Bow shock outside the nozzle decelerate them significantly. It can be seen from Fig. 8 that the impinging velocity of 0.5 μm diameter copper particles on the substrate is below 50 m/s. Apparently, this velocity is virtually impossible to deposit the particle on the substrate. Nevertheless, the situations of platinum particles under the same conditions are somewhat different; as shown in Fig. 9 the impinging velocities are much higher than that of copper particles for smaller particles; the result indicates that the velocity of 0.5 μm diameter platinum particles on the substrate nearly approach to 500 m/s. But the velocities of large platinum particles, such as 25 μm and 50 μm diameter, are lower than that of copper particles with same diameters under the same conditions because of the higher density of platinum particles.

The simulation results for the carrier gas of He are illustrated in Figs. 10 and 11. From the figures, it can be seen that He gas can be accelerated to much higher speed (about two times fasters when compares to N_2 carrier gas shown in Figs. 8 and 9) and the cone-shape shocks formed at the location of the connection between the divergent section and the straight section in the nozzle are very strong at the beginning, then decay quickly as flowing downstream. It is observed from Fig. 10 that

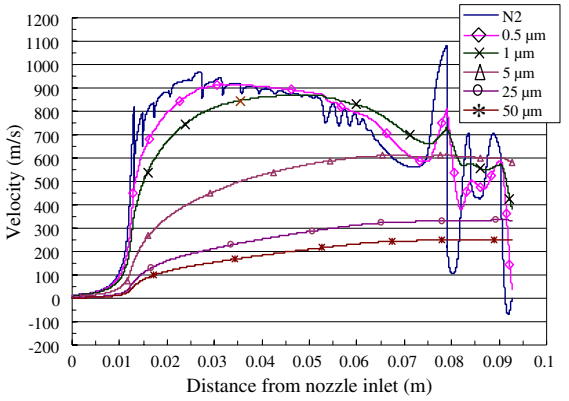

Fig. 8. The velocity of copper particles with different diameters in N_2 gas stream.

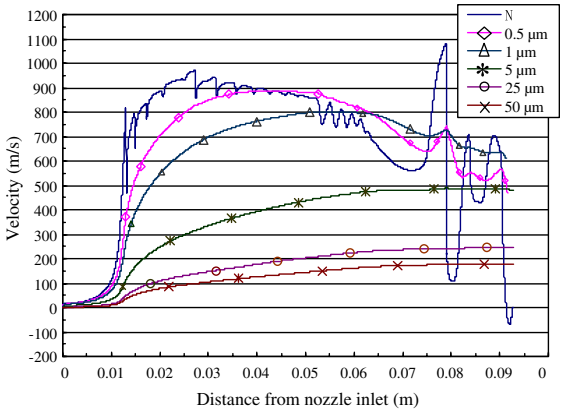

Fig. 9. The velocity of platinum particles with different diameters in N_2 gas stream.

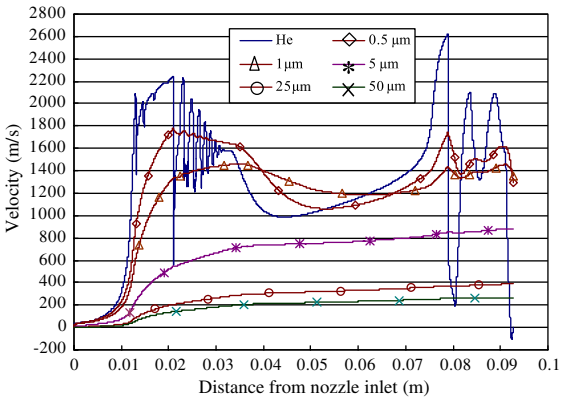

Fig. 10. The velocity of copper particles with different diameters in He gas stream.

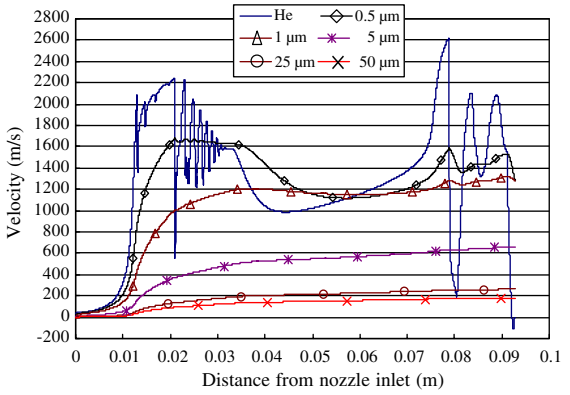

Fig. 11. The velocity of platinum particles with different diameters in He gas stream.

the copper particle of 0.5 μm diameter reduces its velocity as it passes through the cone-shaped shocks which are located in the region of 0.02–0.03 m. For platinum particle in the same situation (see Fig. 11), the reduction of its velocity is not as significant as copper particle. Compared with N_2 as carrier gas, He carrier gas has much better acceleration performance, especially for smaller particles. The particle velocity distribution on the centerline for N_2 and He as carrier gas indicates that the nozzle length, in particular the extended straight section, is too long for smaller particles (smaller than 1 μm). The results also show that the extended straight section may have different optimal length for different size of the particles, and may be even unnecessary for sub-microsize particle, which is strikingly different from the results of the previous investigations [3].

As to the nano-scale particle, such as 100 nm, the trajectory tracking of platinum particle in N_2 gas stream is shown in Fig. 12. The result implies that the particle with 100 nm diameter cannot perforate the Bow shock. It is forced to pass by Bow shock and turns around the vortex as shown in Fig. 7. Therefore, in order to make particles of 100 nm diameter or smaller size has enough momentum (velocity) to penetrate the Bow shock, the nozzle inlet gas pressure (and temperature) needs to increase to a much higher value or other complemented acceleration approaches (e.g., electric field or magnetic field) have to be used to significantly increase the particle velocity.

Figs. 13 and 14 demonstrate the comparisons of velocities of 0.5 μm and 5 μm diameter copper and platinum particles accelerated by N_2 and He carrier gas respectively. It is clearly observed that the densities of particles have significant effect on the acceleration of bigger particles. Higher density particle (Pt) has a smaller acceleration in the nozzle due to its larger mass, and the lighter particle (Cu) accelerates fast due to its smaller mass. Nevertheless, this effect almost disappears when the particle size decreases to 0.5 μm (500 nm) diameter or less.

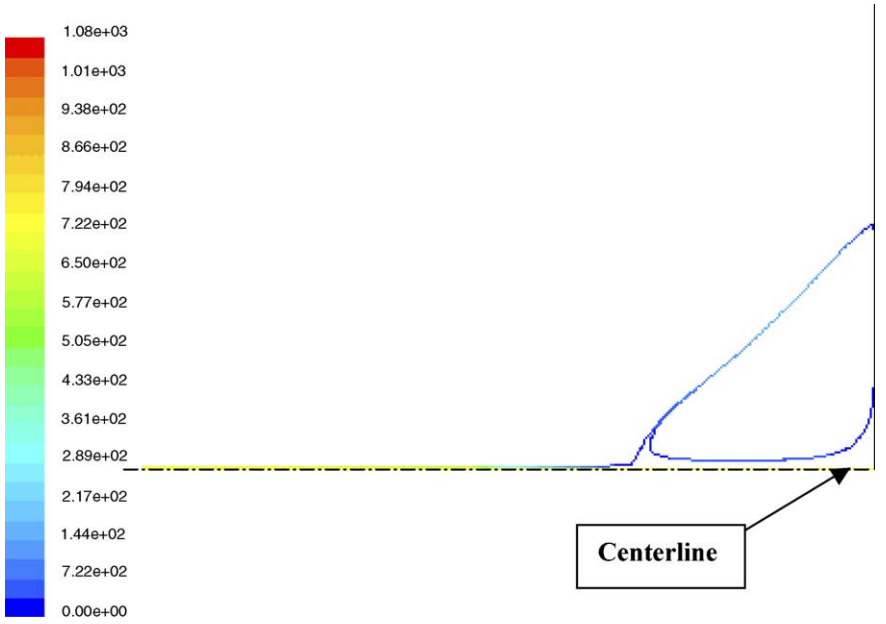

Fig. 12. The particle tracking of platinum with 100 nm diameter.

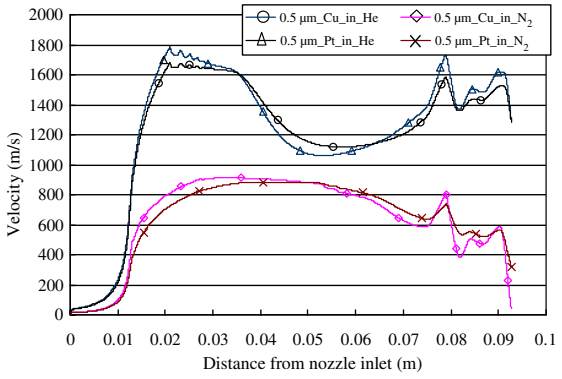

Fig. 13. The velocity comparison of copper and platinum particle with 0.5 μm diameter.

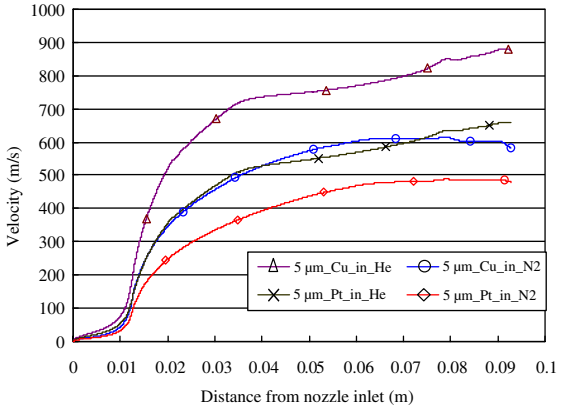

Fig. 14. The velocity comparison of copper and platinum particle with 5 μm diameter.

5. Conclusions

1. A small turn angle at the location of the connection between the divergent section and the following straight section caused cone-shape weak shocks (compression waves), which results in the centerline velocity of carrier gas (N_2 or He) fluctuating in the straight section of nozzle.
2. The friction in the straight extended section causes the gas velocity of carrier gas decreases considerably.
3. The Barrel shock of underexpanded flow appears outside the nozzle. Along the jet, the shear layer grows and penetrates further into the jet core because of the entrainment of the gas outside the shear layers.
4. Between nozzle exit and the substrate, there exists a well-formed Mach disk located close to the nozzle exit, a subsequent second weaker Mach disk and a Bow shock formed on the substrate.
5. A vortex is formed in the region closed by Bow shock and the substrate and the pressure in this closed region is much higher. The flow direction around the centerline in the vortex is opposite the direction of the main jet stream.
6. The cone-shape weak shocks inside the nozzle, the Mach disk and Bow shock outside the nozzle almost have no effect on the acceleration of copper particles with diameter more than 5 μm. Although the cone-shape weak shocks inside the nozzle cannot slow down the smaller particles, such as 1 μm and 0.5 μm diameter particles, the Mach disk and Bow shock outside the nozzle decelerate them significantly. The impinging velocity of 0.5 μm diameter copper particles on the substrate is below 50 m/s in the case study.
7. For smaller particles, the impinging velocities of platinum particles under the same conditions are much higher than that of copper particles. The velocity of 0.5 μm diameter platinum particles on the substrate nearly approach to 500 m/s. But the velocities of large platinum particles, such as 25 μm and 50 μm diameter, are lower than that of copper particles with same diameters under the same conditions.
8. He gas can be accelerated to a very high speed. Although the cone-shape shocks formed at the location of the connection between the divergent section and the straight section in the nozzle are very strong at the beginning, then decay quickly as flowing downstream.When compared He carrier gas with N_2 carrier gas, He gas has much better acceleration performance, especially for smaller particles.
9. A longer nozzle (i.e. longer straight section) is useful only to the acceleration of bigger particles. The extended straight section may have different optimal length for different size of the particles, and may be even unnecessary for sub-microsize particle.
10. The particle with 100 nm diameter cannot perforate the Bow shock. It was forced to pass by Bow shock and turns around the vortex.
11. The densities of particles have significant effect on the acceleration of bigger particles. Higher density particle (Pt) has a smaller acceleration in the nozzle due to its larger mass, and the lighter particle (Cu) accelerates fast due to its smaller mass. Nevertheless, this effect almost disappears when the particle size decreases to 0.5 μm (500 nm) diameter or less.

Acknowledgements

The authors, Qinghua Chen and Longjian Lee, acknowledge the support of this work by China National Natural Science Foundation Grant No. 50276073. Dr. Tien-Chien Jen and Mr. Qinghua Chen would also like to acknowledge the partial financial support from National Science Foundation DMII GOALI grant-9908324.

Appendix A

The drag coefficient equation (12) used are

$$C_D = \frac{24.0}{Re} \quad \text{for } Re < 0.1,$$

$$C_D = 3.69 + \frac{22.73}{Re} + \frac{0.0903}{Re^2} \quad \text{for } 0.1 < Re < 1,$$

$$C_D = 1.222 + \frac{29.1667}{Re} - \frac{3.8889}{Re^2} \quad \text{for } 1 < Re < 10.0,$$

$$C_D = 0.6167 + \frac{46.5}{Re} - \frac{116.67}{Re^2} \quad \text{for } 10.0 < Re < 100.0,$$

$$C_D = 0.3644 + \frac{98.33}{Re} - \frac{2778}{Re^2} \quad \text{for } 100.0 < Re < 1000.0,$$

$$C_D = 0.357 + \frac{148.62}{Re} - \frac{4.75 \times 10^4}{Re^2}$$
for $1000.0 < Re < 5000.0$,

$$C_D = 0.46 - \frac{490.546}{Re} + \frac{57.87 \times 10^4}{Re^2}$$
for $5000.0 < Re < 10000.0$,

$$C_D = 0.5191 - \frac{1662.5}{Re} + \frac{5.4167 \times 10^6}{Re^2}$$
for $10000.0 < Re < 50000.0$.

References

[1] A.P. Alknimov, V.F. Kosarev, A.N. Apayrin, A method of cold gas dynamic deposition, Dokl Acad. Nauk SSSR 318 (1990) 1062–1065.
[2] R.C. McCune, A.N. Papyrin, J.N. All, W.L. Riggs, P.H. Zajchowski, An exploration of the cold gas dynamic spray method for several materials systems, in: Proceedings of the 8th National Thermal Spray Conference, Houston, Texas, 1995, pp. 1–5.
[3] R.C. Dykhuizen, M.F. Smith, Gas dynamic principles of cold spray, J. Thermal Spray Technol. 7 (2) (1998) 205–212.
[4] M. Jicha, K.C. Karki, S.V. Patankar, Numerical analysis of water spray system in the entrance region of a two-dimensional channel using Lagrangian approach, Numer. Heat Transfer, Part A 26 (1) (1994) 1–16.
[5] Z. Liu, R.D. Reitz, Modeling fuel spray impingement and heat transfer between spray and wall in direct injection diesel engines, Numer. Heat Transfer, Part A: Applications 28 (5) (1994) 515–529.
[6] Y.M. Kim, S.J. Kim, Z.J. Chen, C.P. Chen, Numerical simulation of combustion wave propagation in an air–fuel spray mixture with temperature nonuniformity, Numer. Heat Transfer, Part A: Applications 34 (1) (1998) 23–41.
[7] J.F. Wiedenhoefer, R.D. Reitz, Modeling the effect of EGR and multiple injection schemes on IC engine component temperatures, Numer. Heat Transfer, Part A: Applications 37 (7) (2000) 673–694.
[8] M.S. Raju, Application of scalar Monte Carlo probability density function method for turbulent spray flames, Numer. Heat Transfer, Part A: Applications 30 (8) (1996) 753–777.
[9] X. Yang, S. Eidelman, Numerical analysis of a high-velocity oxygen-fuel thermal spray system, J. Thermal Spray Technol. 5 (2) (1996) 175–184.
[10] S. Roychoudhary, T.L. Bergman, Response of agglomerated, multiceramic particles to intense heating and cooling for thermal plasma spraying simulation, Numer. Heat Transfer, Part A: Applications 45 (3) (2004) 211–233.
[11] S. Eidelman, X. Yang, Optimization of thermal spray guns and coating processes using numerical simulations, in: Proceedings of the 1996 125th TMS Annual Meeting, Anaheim, CA, USA, 1996, pp. 47–57.
[12] X. Yang, S. Eidelman, Analysis of thermal spray systems by comprehensive numerical simulations, in: Proceedings of the 1996 125th TMS Annual Meeting, Anaheim, CA, USA, 1996, pp. 755–769.
[13] K. Sakaki, Y. Shimizu, Effect of the increase in the entrance convergent section length of the gun nozzle on the high-velocity oxygen fuel and cold spray process, J. Thermal Spray Technol. 10 (3) (2001) 487–496.
[14] A.P. Alkhimov, V.F. Kosarev, S.V. Klinkov, The features of cold spray nozzle design, J. Thermal Spray Technol. 10 (2) (2001) 375–381.
[15] Y.F. Wang, X.F. Wang, Z.Y. Huang, X.M. Wang, Numerical simulation of supersonic jet field in cold spray technique for material modification, J. Dalian Univ. Technol. (in Chinese) 44 (3) (2004) 398–401.
[16] W.Y. Li, J.C. Li, Optimization of spray conditions in cold spraying based on numerical analysis of particle velocity, Trans. Nonferrous Met. Soc. China (Engl. Ed.) 14 (Suppl. 2) (2004) 43–48.
[17] Z. Li, J. Zhu, C. Zhang, Numerical simulations of ultrafine powder coating systems, Powder Technol. 150 (2005) 155–167.
[18] Y.Y. Yen. Available from: <http://rat.liv.ac.uk/research/cgdm>.
[19] V. Yakhot, S.A. Orszag, Renormalization group analysis of turbulence: I. Basic theory, J. Scient. Comput. 1 (1) (1986) 1–51.
[20] S.A. Morsi, A.J. Alexander, An investigation of particle trajectories in two-phase flow systems, J. Fluid Mech. 55 (2) (1972) 193–208.
[21] H. Ounis, G. Ahmadi, J.B. McLaughlin, Brownian diffusion of submicrometer particles in the viscous sublayer, J. Colloid Interface Sci. 143 (1) (1991) 266–277.

[22] A. Li, G. Ahmadi, Dispersion and deposition of spherical particles from point sources in a turbulent channel flow, Aerosol Sci. Technol. 16 (1992) 209–226.

[23] R.M. Rhie, W.L. Chow, Numerical study of the turbulent flow past an airfoil with trailing edge separation, AIAA J. 21 (11) (1983) 1525–1532.